

Phase-field model for Hele–Shaw flows with arbitrary viscosity contrast II: numerical study

R. Folch, J. Casademunt, A. Hernández–Machado
Departament d'Estructura i Constituents de la Matèria
Universitat de Barcelona, Av. Diagonal, 647, E-08028-Barcelona, Spain

L. Ramírez–Piscina
Departament de Física Aplicada
Universitat Politècnica de Catalunya, Av. Dr. Marañón, 50, E-08028-Barcelona, Spain

Abstract

We implement a phase-field simulation of the dynamics of two fluids with arbitrary viscosity contrast in a rectangular Hele-Shaw cell. We demonstrate the use of this technique in different situations including the linear regime, the stationary Saffman-Taylor fingers and the multifinger competition dynamics, for different viscosity contrasts. The method is quantitatively tested against analytical predictions and other numerical results. A detailed analysis of convergence to the sharp interface limit is performed for the linear dispersion results. We show that the method may be a useful alternative to more traditional methods.

Typeset using REVTeX

I. INTRODUCTION

In the previous paper [1] we presented a phase-field model for the Saffman–Taylor problem with arbitrary viscosity contrast. The problem consists in determining the time evolution of the interface between two immiscible (viscous) fluids within a Hele–Shaw cell [2]. This can be done analytically only in very restricted situations, so numerical work is usually required. As other free boundary problems (bulk problems with boundary conditions on a moving boundary), Hele–Shaw flows have traditionally been formulated by projecting the bulk dynamics onto the interface using boundary-integral methods which lead to integro-differential equations [3–8]. An alternative approach, namely the so-called phase-field model, has also been used to study solidification and related problems [9–16]. This approach describes the system in terms of a set of partial differential equations avoiding the treatment of the interface as a moving boundary. To do so, an additional field is introduced which locates the interface at a region of thickness ϵ . The equations are then required to yield the original moving-boundary problem in the sharp interface limit $\epsilon \rightarrow 0$. For Hele–Shaw flows, such a phase-field model was introduced in Ref. [1]. In this case two independent small parameters (ϵ and $\tilde{\epsilon}$) were actually introduced, over which three distinct conditions control the convergence to the sharp-interface limit $\epsilon, \tilde{\epsilon} \rightarrow 0$. In the paper we proved that model to yield the right sharp-interface equations in this limit and obtained a ‘thin-interface’ model, which consists of a set of effective sharp-interface equations which keep finite- ϵ and $-\tilde{\epsilon}$ effects up to first order. This provides appropriate criteria to choose the computational parameters for numerical simulations, and, for the linear regime, it enables to explicitly compute deviations from the Hele–Shaw growth rates.

The purpose of the present paper is to numerically check the phase-field model, and eventually the corresponding thin-interface approximation, against known sharp-interface solutions, and to assess its usefulness in practice. Indeed, the fact that the model has the correct sharp-interface limit does not guarantee its practical usefulness for several reasons. On the one hand, the stability of both the bulk phases and the kink profile must be assured, since this might not be the case in general. On the other hand, a direct empirical test is necessary to determine quantitatively how close a finite ϵ situation is to the sharp-interface limit. This means finding a set of explicit quantitative criteria to choose all the nonphysical parameters in order to ensure a desired accuracy. Finally, it is interesting to evaluate the capability of that model at providing quantitative results with reasonable computing efforts in actual simulations.

The rest of the paper is organized as follows: In Sec. II we present the phase-field equations and the boundary conditions, discretization and parameters used. Some preliminary tests on phase conservation are carried out in Sec. III. In Sec. IV we show how to choose these computational parameters in the linear regime and how to obtain the growth rates in the numerical linear dispersion relation, which we compare satisfactorily with the sharp interface limit and with a thin-interface model. Convergence with these parameters is also tested. Sec. V is devoted to the steady state. Saffman–Taylor fingers are obtained from single-mode initial conditions in the non-linear regime, and their velocities and widths are compared with previous results. Multifinger configurations arising from a random initial condition in the linear regime are obtained in Sec. VI, which are morphologically and dynamically consistent with existing evidence both from experiments [17] and simulations [6].

Finally, we discuss the applicability of the model and its possible future extensions in Sec. VII.

II. IMPLEMENTATION OF THE MODEL

We will consider a rectangular Hele–Shaw cell of width W (x -direction) and gap b (z -direction), containing two fluids with distinct viscosities (μ_1, μ_2) and densities (ρ_1, ρ_2) . Both fluids are separated by an interface with surface tension σ , and move under an effective gravity g_{eff} (negative y -direction) and an injection velocity V_∞ (positive y -direction). It is convenient to introduce the stream function ψ as the harmonic conjugate, which can be defined by $u_x = \partial_y \psi$, $u_y = -\partial_x \psi$, where u_x, u_y are the x, y components of the fluid velocity field \vec{u} . In terms of the stream function the governing equations in dimensionless form read

$$\nabla^2 \psi = 0 \quad (2.1)$$

$$\psi_r(0^+) - \psi_r(0^-) = -\gamma - c[\psi_r(0^+) + \psi_r(0^-)] \quad (2.2)$$

$$\psi_s(0^+) = \psi_s(0^-) = -v_n, \quad (2.3)$$

where r (resp. s) is a coordinate normal (tangential) to the interface, 0^\pm means on the interface coming from either fluid, the subscripts stand for partial derivatives except for $v_n(s)$, which is the normal velocity of the interface, and

$$\frac{\gamma(s)}{2} \equiv B\kappa_s + \hat{y} \cdot \hat{s}, \quad (2.4)$$

with $\kappa(s)$ the interface curvature. The dynamics are controlled by the two dimensionless parameters

$$B = \frac{b^2 \sigma}{12W^2[V_\infty(\mu_1 - \mu_2) + g_{eff} \frac{b^2}{12}(\rho_1 - \rho_2)]}, \quad c = \frac{\mu_1 - \mu_2}{\mu_1 + \mu_2}. \quad (2.5)$$

Here, c is the viscosity contrast, that without loss of generality is taken as positive ($0 \leq c \leq 1$), and B is a dimensionless surface tension, measuring the ratio between the stabilizing force of the capilarity and the destabilizing driving force induced by injection and gravity. We will restrict ourselves to the unstable case, i.e. positive values of B . The equations are then written in the frame moving with the fluid at infinity (or, equivalently, with the mean interface), and taking W as the length unit and $U_* \equiv cV_\infty + g_{eff} \frac{b^2(\rho_1 - \rho_2)}{12(\mu_1 + \mu_2)}$ the velocity unit (see [3]).

The corresponding phase-field model which we have used was proposed in [1], with θ the phase field:

$$\tilde{\epsilon} \frac{\partial \psi}{\partial t} = \nabla^2 \psi + c \vec{\nabla} \cdot (\theta \vec{\nabla} \psi) + \frac{1}{\epsilon} \frac{1}{2\sqrt{2}} \gamma(\theta)(1 - \theta^2) \quad (2.6)$$

$$\epsilon^2 \frac{\partial \theta}{\partial t} = f(\theta) + \epsilon^2 \nabla^2 \theta + \epsilon^2 \kappa(\theta) |\vec{\nabla} \theta| + \epsilon^2 \hat{z} \cdot (\vec{\nabla} \psi \times \vec{\nabla} \theta) \quad (2.7)$$

where $f(\theta) \equiv \theta(1 - \theta^2)$, and $\frac{\gamma(\theta)}{2} \equiv \hat{s}(\theta) \cdot (B \vec{\nabla} \kappa(\theta) + \hat{y})$, $\kappa(\theta) \equiv -\vec{\nabla} \cdot \hat{r}(\theta)$, with $\hat{r}(\theta) \equiv \frac{\vec{\nabla} \theta}{|\vec{\nabla} \theta|}$ and $\hat{s}(\theta) \equiv \hat{r}(\theta) \times \hat{z}$, together with the boundary condition

$$\theta(y \rightarrow \pm\infty) = \pm 1, \quad (2.8)$$

where $\theta = +1(-1)$ corresponds to fluid 1 (2).

$\tilde{\epsilon}$ can be regarded as a diffusion time of the stream function over a characteristic length of wavenumber k , $\frac{\tilde{\epsilon}}{(1 \pm c)k^2}$ (which must be chosen much smaller than the characteristic inverse growth rate of the corresponding mode of the interface $|\omega|^{-1}$). On the other hand ϵ is basically the interface thickness (which is required to be much smaller than the length scale $|k|^{-1}$). ϵ^2 also stands for the relaxation time of the phase field towards the kink profile, which in turn must be kept well below the inverse growth rate $|\omega|^{-1}$ (see Ref. [1]. Sec. IV). These inequalities control the convergence to the Hele–Shaw dynamics, and, for the linear regime, the deviation from it can be computed analytically from them (see Ref. [1]. Sec. IV), thus providing *a priori* criteria for the choice of $\tilde{\epsilon}$ and ϵ to obtain a prescribed accuracy.

To be consistent with the frame change and adimensionalization inherent to the parameters B and c previously defined we use a cell of width 1, with periodic boundary conditions in the x -direction (which include rigid walls as a particular case) and no flux (constant stream function, e.g. $\psi = 0$) in the y -direction. Whenever some symmetry of an initial condition exists and is preserved by the time evolution, we use a properly reduced integration domain (e.g. left-right symmetry for a single mode, or up-down symmetry for an up-down symmetric initial condition with $c = 0$).

Numerical integration of the above equations has been carried out on a grid of size $n_x \times n_y$ with equal spacing $\Delta x = \Delta y = 1/n_x$ in both x and y directions, using an explicit centered-space algorithm. n_x is chosen so that Δx at most equals ϵ for the profile of the fields across the interface to be properly resolved. The ϵ value thus constrains Δx and, in turn, the minimum size of the system and the maximum time step, so that the computing time required to integrate a certain physical dynamics goes as ϵ^{-4} . Then n_y is chosen so that there is always a distance of at least one of the largest present wavelengths between the interface and the $\psi = 0$ boundary condition at the end of the channel. An increase in this distance does not seem to affect appreciably the interface evolution. This is what expected in the linear regime, where the stream function decays exponentially with the present wavelengths, but is an *a posteriori* observation for the Saffman–Taylor fingers.

As for the initial condition, in general one should set the phase field to $\theta = \tanh \frac{r}{\sqrt{2\epsilon}}$, with r being the signed distance to the desired interface, which is the model solution at least up to first order in ϵ (see Ref. [1]). Then the corresponding stream function should be close to the stationary solution of Eq. (2.6) for that phase field. This can be obtained either by solving the stationary version of Eq. (2.6) (a Poisson equation) or by letting the stream function in Eq. (2.6) relax while keeping the phase field frozen. However in the present paper, since we will consider perturbed planar interfaces as initial situations, we will make use of the fields predicted by the linear theory: $\theta = \tanh \frac{y}{\sqrt{2\epsilon}}$, where y is signed vertical distance to the desired interface, and the thin-interface result (see Ref. [1])

$$\psi(x, y) = a_{\pm} A e^{ikx - q_{\pm}|y|}, \quad (2.9)$$

with

$$a_{\pm} = \frac{i\omega_0}{k} \left(\frac{1}{\sqrt{1 + \frac{\tilde{\epsilon}\omega}{k^2}}} \mp c\epsilon|k|\sqrt{2} \right) + \mathcal{O}(c^2) + \mathcal{O}(\epsilon^2). \quad (2.10)$$

and

$$q_{\pm} = \left| k \sqrt{1 + \frac{\tilde{\epsilon}\omega}{k^2(1 \pm c)}} \right|. \quad (2.11)$$

III. PHASE CONSERVATION

Before testing the model in physical situations a preliminary test is that of the conservation of the two fluid phases. Due to incompressibility and immiscibility, the Hele–Shaw dynamics preserve the area and phase purity of each domain. In contrast, model A, starting point for the equation for the phase-field Eq. (2.7) (see Ref. [1]), does not even preserve the global balance between phases. For reasonable values of the interface thickness ϵ these non-conserved dynamics are given approximately by Allen–Cahn law ($v_n \propto \kappa$). Thus, phase-conservation within the phase-field scheme depends on the accuracy of both the $\epsilon^2 \kappa(\theta) |\vec{\nabla}\theta|$ term in cancelling out Allen–Cahn law and the coupling $\hat{z} \cdot (\vec{\nabla}\psi \times \vec{\nabla}\theta)$ in introducing the Hele–Shaw dynamics.

First, we test Allen–Cahn law cancellation by considering situations in which the stream function drops from the equations. For a circular droplet of one phase embedded in the other in absence of gravity Eq. (2.7) reduces to $\epsilon^2 \frac{\partial\theta}{\partial t} = f(\theta) + \epsilon^2 \frac{d^2\theta}{dr^2}$ (because $\frac{\partial\theta}{\partial s} = 0$), where r is the radial coordinate. This is exactly model A in one dimension, and therefore Allen–Cahn law cannot arise. Starting with $\theta = \tanh \frac{r}{\sqrt{2}\epsilon}$ as initial condition, there is some slow dynamics which soon gets stacked because of the limited numerical resolution. From then on, the fluid phases are completely conserved. In contrast, if the term cancelling out Allen–Cahn law is removed from Eq. (2.7), the droplet quickly collapses.

The same test can be carried out for a marginal mode in a nearly flat interface with identical results: If the Allen–Cahn law correction is removed, the mode quickly flattens, whereas, if it is not, some slow dynamics soon gets stacked within the numerical resolution. This corresponds to the point $k' = 1$ in Fig. 2 (see next section), whose measured growth rate ω' vanishes exactly. Both tests suggest that the $\epsilon^2 \kappa(\theta) |\vec{\nabla}\theta|$ term cancels out Allen–Cahn law even at higher orders in ϵ than those computed in Ref. [1].

As for general situations in which the coupling term can also play a role, significant violation of phase conservation has only been observed for such large values of ϵ that $\epsilon\kappa > 1$. We therefore conclude that the two fluid phases are conserved for reasonable values of ϵ , and that, in practice, this is not a restrictive condition on ϵ .

IV. LINEAR DISPERSION RELATION

The first physically relevant situation in which we have tested the model is the linear regime of a perturbed planar interface. The linear dispersion relation has been computed for vanishing viscosity contrast ($c = 0$). Sharp-interface model predicts a linear growth that does not depend on c . However, the phase field model should exhibit some dependence in the viscosity contrast related to the finite- ϵ and $-\tilde{\epsilon}$ corrections (see Ref. [1]. Sec. IV).

We use a single mode occupying the whole channel width (i.e., of wavelength 1 and wavevector $k = 2\pi$) and then vary the dimensionless surface tension B in order to change the growth rate of that mode according to the Hele–Shaw dispersion relation

$$\omega_0 = |k|(1 - Bk^2). \quad (4.1)$$

This is physically completely equivalent to fixing the surface tension and varying the wavevector of the mode, as can be seen through the rescaling $k' = \sqrt{B}k, \omega'_0 = \sqrt{B}\omega_0 = |k'|(1 - k'^2)$. However, it is numerically more convenient, since it allows one to use the same value of ϵ for all the modes, because k is fixed. Thus, according to the finite- ϵ and $-\tilde{\epsilon}$ dispersion relation derived in Ref. [1]

$$\omega = \omega_0 \left(\frac{1}{\sqrt{1 + \frac{\tilde{\epsilon}\omega}{k^2}}} - \epsilon |k| \sqrt{2\frac{5}{6}} \right) + \mathcal{O}(c^2) + \mathcal{O}(\epsilon^2). \quad (4.2)$$

We have used $\epsilon = 0.01$, $\tilde{\epsilon} = 0.1$ in order to keep the deviation from the sharp-interface one, ω_0 , below a 10% (we have used its maximum, $\omega = 2\pi$, to compute the required value of $\tilde{\epsilon}$). Finally, the initial amplitude of the mode is chosen to equal the mesh size Δx —which in turn is set to $\epsilon/2$ for reasons explained below—, so that we stay for a while in the linear regime for unstable modes, and yet we have enough numerical subgrid resolution for the stable ones also for a while.

The time evolution of a relevant mode (one close to the most unstable one), with $B = 6.5 \times 10^{-3}$, is shown in Fig. 1. The points (+) have been obtained by averaging the ratio of the interface height y at a certain time t and the initial one $y(0)$ over 1/4th of the interface. The slope of the resulting curve in a linear-log plot is the growth rate. Where this is constant, the growth is exponential and we are in the linear regime. This corresponds to the linear fit plotted in Fig. 1., from which we obtain the growth rates shown in Fig. 2. Beyond this regime the points curve down because of the non-linearities. The crossover corresponds to an amplitude of about a tenth of the wavelength of the mode.

The behaviour of the stream function has been plotted in a dotted line for purposes of comparison. According to the linear theory (see, e.g. [1]), the absolute value of the stream function at any point of the system should also grow exponentially with the same growth rate than the interface, and this is indeed the case, since the dotted line—average over the whole bulk of the absolute value of the ratio between the stream function ψ in a certain point at a certain time t and the initial one at the same point $\psi(0)$ — is parallel to the interface evolution in the linear regime. The gap between the two straight lines is due to the initial, very short—and therefore not visible in the figure— decay of the stream function, which reflects the rounding on a scale of $\mathcal{O}(\epsilon)$ of the gradient on the interface of the sharp-interface result used as initial condition.

In Fig. 2 we present the linear dispersion relation thus obtained in the rescaled variables defined above. The points (+) correspond to the growth rates measured as in Fig. 1, for times ranging from 0.3 to 0.7, i.e., for roughly a decade in the amplitude. Their deviation from the sharp-interface result of Eq. (4.1) (solid line) keeps below the desired 10% error and is fairly well quantitatively predicted by the thin-interface dispersion relation of Eq. (4.2) (dotted line). This quantitative agreement between theory and numerics is quite remarkable if we take into account that the thin-interface model is based on an asymptotic expansion in ϵ . This good agreement is indeed an indication that the value of ϵ used is in the asymptotic regime of the sharp-interface limit, as we will see more clearly in Fig. 3.

Although we in fact introduce the thin-interface growth rate Eq. (4.2) into the initial condition for the stream function, the results do not depend on this after a certain transient. If one sets more naively the sharp-interface growth rate ω_0 into the initial condition for the stream function, one gets a rather long transient in which the slope of an amplitude-time log-linear plot like that of Fig. 1 initially curves down (up) for an unstable (stable) mode, i.e., the growth is not exponential, and we are therefore not describing properly the Hele–Shaw problem. The slope then relaxes towards the thin-interface one and the growth becomes exponential, but non-linearities soon set in. In contrast, if the thin-interface growth rate is set into the initial stream function, one gets constant slopes from the very beginning. This allows one to measure the growth rate in a wider range of time and is indeed also an indication that the thin-interface model is valid.

The growth rate values shown in Fig. 2 could still be refined by further decreasing ϵ and $\tilde{\epsilon}$. This is not only a theoretical possibility, but can also be done in practice as we show in Fig. 3, although the computation time increases as explained above. Here, we study the convergence of the growth rate ω (y-axis) for the maximum of $\omega'(k')$ ($B = 8.443 \times 10^{-3}$) to the Hele–Shaw result $\omega_0 = 4.188$ (left upper corner) as we decrease ϵ (x-axis) and $\tilde{\epsilon}$ (various symbols). The empty symbols have been obtained with $\Delta x = \epsilon$, whereas the filled ones correspond to $\Delta x = \epsilon/2$. The growth rates obtained with $\Delta x = \epsilon$ are always below the ones for $\Delta x = \epsilon/2$, probably because of the stabilizing effect of the mesh size. If Δx is further decreased the differences with the values computed with $\Delta x = \epsilon/2$ are tiny, whereas the gap between the $\Delta x = \epsilon$ and the $\Delta x = \epsilon/2$ points is pretty large (clearly more than the differences between distinct symbols —distinct $\tilde{\epsilon}$ values— or adjacent values of ϵ). This means that the discretization has practically converged to the continuum model for $\Delta x = \epsilon/2$, but not for $\Delta x = \epsilon$. That is the reason why we have used $\Delta x = \epsilon/2$ in Figs. 1 and 2.

Moreover, the $\Delta x = \epsilon/2$ points should be described by the thin-interface model of Eq. (4.2), and this is indeed the case for small enough values of ϵ . To visually see this we have plotted the thin-interface prediction for $\tilde{\epsilon} = 0$ (dashed line), which is, of course, a straight line in ϵ . Each set of points with the same $\tilde{\epsilon}$ value clearly tend to allign parallel to this line as ϵ decreases —as Eq. (4.2) predicts—, whereas they curve up and even cross the line for large values of ϵ , for which we are beyond the asymptotic regime of validity of Eq. (4.2), apparently ending near $\epsilon = 0.01$. This makes $\epsilon = 0.01$ very suitable for simulations, and confirms it to be within the asymptotic regime as we pointed out above. Note as well how the growth rate increases with decreasing values of $\tilde{\epsilon}$ within the same value of ϵ (vertical columns of points), and how it approaches the dashed line in good agreement with the values predicted by Eq. (4.2) for values of ϵ within the asymptotic regime.

V. SAFFMAN–TAYLOR FINGERS

Once the model has been tested in the linear regime, it seems mandatory to check a highly non-linear situation such as the steady state, for which many analytical and numerical results are available.

We start with a single mode occupying the whole channel and with an amplitude equal to the channel width, i.e., clearly in the non-linear regime. Obviously the initial condition predicted by the linear theory is not accurate, but this just introduces a transient during which the dynamics is not the Hele–Shaw one. By the time the forming finger is close to the steady shape, all transients must have decayed. Moreover, starting with a single mode we not only check that the model exhibits a finger solution, which we could do much faster by starting with that solution, but that the model is robust to inaccurate initial conditions for the bulk, and also that single fingers have a reasonable basin of attraction, which may be a rather nontrivial point for small c [6].

Here we do not have a theoretical prediction for the deviations from the Hele–Shaw steady state due to finite- ϵ and $-\tilde{\epsilon}$ effects. However, we know that the inequalities of Sec. II still control the convergence. The differences are that ω now stands for the steady advance velocity (which should be in the range 0.7-0.8, not far from the maximum growth rate in the linear regime $\omega = 2\pi$), and that all unstable modes—and not only the one set by the initial condition—are present in the steady state, so that k must be chosen to be the less favourable in each inequality. This continues to be $k = 2\pi$ for the condition on $\tilde{\epsilon}$, but becomes $k = 1/\sqrt{3B}$, the most unstable mode, for the one on ϵ . We thus progressively decrease the values of ϵ and $\tilde{\epsilon}$ and look for convergence (in the finger widths) within the computational resources.

The finest comparable simulation runs are shown in Figs. 4.a-d. For $B = 10^{-2}$ (Figs. 4.a-c) we have used $\epsilon = 0.02$, twice less accurate than the one used in the linear regime (Figs. 1-2), whereas for $B = 10^{-3}$ (Fig. 4.d) $\epsilon = 0.01$, three times less accurate. As for $\tilde{\epsilon}$, we have used $\tilde{\epsilon} = 0.2$ for $c = 0$ (Figs. 4.a and 4.d), $\tilde{\epsilon} = 0.1$ for $c = 0.5$ (Fig. 4.b), and $\tilde{\epsilon} = 0.02$ for $c = 0.9$ (Fig. 4.c), all of them twice less accurate than the one in the linear regime. However, convergence in $\tilde{\epsilon}$ seems to be achieved, at least in the finger widths. We cannot assure it for ϵ because the finger tip splits for $B = 10^{-3}$ —probably because of numerical noise—if ϵ is further lowered. In all cases we have used $\Delta x = \epsilon/2$ like in the linear regime tests, although we have found that already for $\Delta x = \epsilon$, the differences in widths are at most within a 1%.

Figs. 4.a-d show single fingers that are formed and relax to a certain width to just advance with a steady velocity. This can be measured plotting the tip position against time, finding excellent linearity from $t = 1.15$ to at least $t = 3.3$ (for the fastest finger). Four successive interfaces at constant time intervals are shown covering this whole regime. Except for the $c = 0.9$ case of Fig. 4.c, the finger has not completely relaxed to its final width for the first plotted interface, which means that we are not in the steady state yet. From the second to the last shown interfaces, no observable change in width, tip velocity or shape is seen anymore. Taking into account that Figs. 4.a-d show the whole channel—although simulations were carried out using half ($c \neq 0$) or a quarter ($c = 0$) of it—it is clear from Fig. 4.d that the end of the channel can be set even closer to the tip of the finger than a channel width (i.e., closer than what the linear regime would have suggested). Regarding

to the values of this steady velocity, they are always a 10-20% below what predicted for an (infinite) Saffman–Taylor finger of the same width without surface tension, although velocity does increase with decreasing finger width as can be seen comparing Figs 4.a and 4.d. The origin of this quantitative discrepancy must lie necessarily on finite- ϵ and $-\tilde{\epsilon}$ effects, most likely related to the non-laplacian character introduced by $\tilde{\epsilon}$, which produces a finite diffusion length.

Note that $c = 0$ fingers (Figs. 4.a and 4.d) are up-down symmetric (also if one uses the whole cell as integration domain), whereas the $c \neq 0$ ones are not, but the less viscous fluid (down, negative y values) propagates into the more viscous one (up, positive y values) in the shape of a Saffman–Taylor finger, whereas the more viscous propagates into the less one in the shape of a drop. If Fig. 4.a is compared to 4.b and 4.c (all with $B = 10^{-2}$ but increasing viscosity contrast c), one sees that the higher the viscosity contrast, the longer the Saffman–Taylor finger and the shorter the drop part (the initial condition was centered about $y=0$). All such dependences on c coincide with Tryggvason and Aref’s observations from their vortex sheet numerical scheme [4].

As for the finger widths, all above 1/2 of that of the channel, they decrease with decreasing dimensionless surface tension B and increasing viscosity contrast c . This c -dependence can also be seen in Fig. 1 of Ref. [4]. Quantitative comparison with McLean–Saffman numerical solvability theory results for $c = 1$ is only feasible to some extent if $c = 1$ widths are extrapolated from the $c \neq 1$ ones obtained, since our model cannot treat the limiting case $c = 1$. By doing this for $B = 10^{-2}$ ($\lambda = 0.63$ for $c = 0$, $\lambda = 0.61$ for $c = 0.5$, and $\lambda = 0.60$ for $c = 0.9$, Figs. 4.a-c), one obtains $\lambda \simeq 0.60$ for $c = 1$, a 6% below the McLean–Saffman value $\lambda = 0.637$. For $B = 10^{-3}$, $c > 0$ fingers would become very computationally demanding, but if the same gap between $c = 0$ and $c = 1$ widths as for $B = 10^{-2}$ is assumed, this would yield $\lambda \sim 0.56$ for $B = 10^{-3}$, $c = 1$, within a 5% distance of the McLean–Saffman value $\lambda = 0.528$. Of course this latter extrapolation is not rigorous, since the differences in width due to the viscosity contrast are likely to diminish with decreasing B , so that they vanish for $B \rightarrow 0$ and $\lambda = 1/2$ is selected for all c , as is generally believed to be the case. In any case, the deviations from the McLean–Saffman results found (within a 5-6%) are surprisingly lower than what the used values of ϵ and $\tilde{\epsilon}$ would have suggested taking into account the observed deviations in the linear regime.

VI. MULTI-FINGER DYNAMICS

We have finally tested the model in the non-linear dynamics appearing between the precedent situations, i.e. after the departure of the linear regime and before reaching the steady state. Here we use a somewhat experimentally realistic initial condition consisting of a superposition of sinusoidal modes with random, uniformly distributed amplitudes between -0.005 and +0.005 for each wavelength $\lambda = 1, \frac{1}{2}, \frac{1}{3}, \dots, \frac{1}{7}$ —i.e., in the linear regime and random phases. For $B = 10^{-3}$ the most amplified of these wavelengths will be $\lambda = \frac{1}{3}$, so that we expect 3 unequal fingers to appear and there is a chance for mode interaction and competition to set in. Wavelengths below $\lambda = 0.161$ are stable and will decay. We include some of them anyway. Then all modes are added up to find the interface position. The stream function predicted by the linear theory is also obtained by adding up each mode’s stream function,

but all with their peaks centered at the same final interface position, to avoid the formation of more than one peak of the stream function across the interface.

Since harmonics of the channel width are present, we have to refine the ϵ used in the linear regime. We use $\epsilon = 0.00625$, with $\Delta x = \epsilon$ to save computation time. The value of $\tilde{\epsilon}$ is quite crude ($\tilde{\epsilon} = 0.5$ for the equal viscosities case $c = 0$, Fig. 5.a), especially for the high viscosity contrast ($c = 0.8$) run (Fig. 5.b) ($\tilde{\epsilon} = 0.2$).

The results are shown in Figs. 5.a,b for $0.15 < t < 1.25$ at constant time intervals 0.1 (dots). The latest interface is emphasized in bold and the solid line corresponds to the initial condition for $t = 0$. As we can see, the initial condition happens to have six maxima. Rather quickly, only three them are left as predicted by linear stability, even before entering the non-linear regime, in which these maxima elongate into well developed fingers. For vanishing viscosity contrast ($c = 0$, Fig. 5.a), there is no apparent competition, in agreement with experimental [17] and numerical [3,6] evidence. Longer and shorter fingers all advance. Shorter fingers might not advance so quickly, but they expand to the sides, so they clearly keep growing. In contrast, starting with the same initial condition that for $c = 0$, the $c = 0.8$ run (Fig. 5.b) shows competition between fingers of the less viscous fluid advancing into the more viscous one —and not the other way round—, as is known to happen in the Hele–Shaw problem. The shorter finger now also expands laterally, but it soon begins to move backwards as a whole. Longer times may lead to the pinch-off of droplets in both cases.

VII. CONCLUDING REMARKS

We have numerically integrated the phase-field model proposed in Ref. [1] for the Hele–Shaw problem in the unstable configuration. Simulations have been carried out in several situations: a circular droplet (to test conservation of each fluid), linear regime of a perturbed planar interface, steady state, and non-linear regime in between. The performed tests guarantee that the model can be used in practice to reproduce the Hele–Shaw dynamics. In the model two small parameters, ϵ and $\tilde{\epsilon}$, whose zero limit correspond to the sharp interface limit, can be independently chosen, being the dynamics well described by the thin-interface model derived in [1]. In general, the conditions on ϵ , $\tilde{\epsilon}$ allow one to control the accuracy of the simulations.

The basic criteria to control the closeness to the sharp interface limit are $\epsilon\kappa \ll 1$, $\frac{\tilde{\epsilon}\omega}{(1\pm c)k^2} \ll 1$. More precisely, we find numerically that the thin-interface model is accurate in the linear regime with an error below 10% if one satisfies the conditions $\epsilon k \leq 0.06$, $\frac{\tilde{\epsilon}\omega}{(1\pm c)k^2} \leq 0.016$. The method could be made more efficient by using an adaptative mesh or (possibly) by cancelling out the corrections to the sharp-interface equations remaining (i.e., other than the Allen–Cahn law) in the thin-interface model. For high viscosity contrasts, $c \sim 1$, a distinct model could possibly be more efficient.

Extensions to less studied, related problems are also enlightened, including the study of noise and spatial disorder (for instance to simulate porous media), the study of liquid crystals and other complex fluids, and problems with a physically diffuse interfaces, such as thermal plumes [18] or motion of the salt/fresh water interface in coastal aquifers.

ACKNOWLEDGEMENTS

We acknowledge financial support from the Dirección General de Enseñanza Superior (Spain), Projects No. PB96-1001-C02-02, PB96-0378-C02-01 and PB96-0241-C02-02, and the European Commission Project No. ERB FMRX-CT96-0085. R.F. also acknowledges a grant from the Comissionat per a Universitats i Recerca (Generalitat de Catalunya).

REFERENCES

- [1] R. Folch, J. Casademunt, A. Hernández-Machado, L. Ramírez-Piscina, (to be published)
- [2] P.G. Saffman and G.I. Taylor, Proc. R. Soc. London A, **245**, 312 (1958); D. Bensimon, L. Kadanoff, S. Liang, B.I. Shraiman and C. Tang, Rev. Mod. Phys., **58**, 977 (1986)
- [3] G. Tryggvason and H. Aref, J. Fluid Mech., **136**, 1-30 (1983)
- [4] G. Tryggvason and H. Aref, J. Fluid Mech., **154**, 287-301 (1985)
- [5] J. Casademunt, D. Jasnow and A. Hernández-Machado, Int. J. Mod. Phys. B **6**, 1647 (1992)
- [6] J. Casademunt and D. Jasnow, Phys. Rev. Lett., **67**, 3677 (1991); Physica D, **79**, 387 (1994)
- [7] D. Jasnow and J. Viñals, Phys. Rev. A, **40**, 3864 (1989); **41**, 6910 (1990)
- [8] T.Y. Hou, J.S. Lowengrub and M.J. Shelley, J. Comp. Phys., **114**, 312 (1994); M.J. Shelley, J. Fluid Mech. **244**, 493 (1992); L. Kondic, M.J. Shelley and P. Palffy-Muhoray, Phys. Rev. Lett., **80**, 1433 (1998)
- [9] J.S. Langer, in *Directions in Condensed Matter Physics*, p.165, Eds. G. Grinstein and G. Mazenko, World Scientific (1986)
- [10] R. Kobayashi, Physica D, **63**, 410 (1993)
- [11] A. Wheeler, B. Murray and R. Schaefer, Physica D **66**, 243 (1993)
- [12] A. Karma and W-J. Rappel, Phys. Rev. E, **53**, 3017 (1996); Phys. Rev. Lett., **77**, 4050 (1996); Phys. Rev. E, **57**, 4323 (1998)
- [13] K. Elder, F. Drolet, J. Kosterlitz and M. Grant, Phys. Rev. Lett., **72**, 677 (1994)
- [14] A. Bosch, H. Müller-Krumbhaar and O. Shochet, Z. Phys. B, **97**, 367 (1995); T. Abel, E. Brener and H. Müller-Krumbhaar, Phys. Rev. E, **55**, 7789 (1997)
- [15] J-L. Mozos and H. Guo, Europhys. Lett., **32**, 61 (1995)
- [16] R. González-Cinca, L. Ramírez-Piscina, J. Casademunt, A. Hernández-Machado, L. Kramer, T.T. Katona, T. Börzsönyi and A. Buka, Physica D **99**, 359-368 (1996); R. González-Cinca, L. Ramírez-Piscina, J. Casademunt, A. Hernández-Machado, T.T. Katona, T. Börzsönyi and A. Buka, J. Crys. Growth **193**, 712 (1998).
- [17] J. V. Maher, Phys. Rev. Lett., **54**, 1498 (1985)
- [18] M. Ben Amar, Phys. Fluids, **4**, 2641 (1992)

FIGURE CAPTIONS

Fig. 1 Measure of the interface growth rate for $B = 6.5 \times 10^{-3}$. Crosses (+) correspond to the average over 1/4th of the interface of $y(t)/y(0)$ ($y \equiv$ interface height) and the dotted line to the average over 1/4th of the bulk of $|\psi(t)/\psi(0)|$. The growth rate is the slope of the linear fit (solid line).

Fig. 2 Linear dispersion relation in appropriate variables (see explanation in text). Crosses (+) represent the growth rates obtained as in Fig. 1. The Hele–Shaw result (solid line) and the thin-interface prediction of Eq. (4.2) (dotted line) are shown for comparison.

Fig. 3 Convergence to the Hele–Shaw value for the maximum of the linear dispersion relation curve, $B = 8.44 \times 10^{-3}$, $\omega_0 = 4.18$, as ϵ (x -axis) and $\tilde{\epsilon}$ (1 for circles, 0.25 for triangles and 0.1 for squares) are decreased. The dashed line corresponds to the thin-interface prediction of Eq. (4.2) for $\tilde{\epsilon} = 0$. Empty symbols have been obtained with $\Delta x = \epsilon$, whereas filled ones used $\Delta x = \epsilon/2$.

Fig. 4 Saffman-Taylor finger advance: 4 successive interfaces at constant time intervals for the regime in which the tip velocity stays constant, $1.15 < t < 3.3$. (a-c) $B = 10^{-2}$, $\epsilon = 0.02$: (a) $c = 0$, $\tilde{\epsilon} = 0.2$ ($\lambda = 0.63$); (b) $c = 0.5$, $\tilde{\epsilon} = 0.1$ ($\lambda = 0.61$); (c) $c = 0.9$, $\tilde{\epsilon} = 0.02$ ($\lambda = 0.60$). (d) $B = 10^{-3}$, $\epsilon = 0.01$, $c = 0$, $\tilde{\epsilon} = 0.2$ ($\lambda = 0.59$).

Fig. 5 Time evolution for $B = 10^{-3}$, $\Delta x = \epsilon = 0.00625$ of an initial condition (solid line) combining $\lambda = 1, \frac{1}{2}.. \frac{1}{7}$ with random, uniformly distributed amplitudes between -0.005 and +0.005. Interfaces at time intervals 0.1 are shown in dotted lines starting at $t = 0.15$. The latest interface shown ($t = 1.25$) is represented in bold. (a) lack of competition for $c = 0$ ($\tilde{\epsilon} = 0.5$); (b) competition for $c = 0.8$ ($\tilde{\epsilon} = 0.2$).

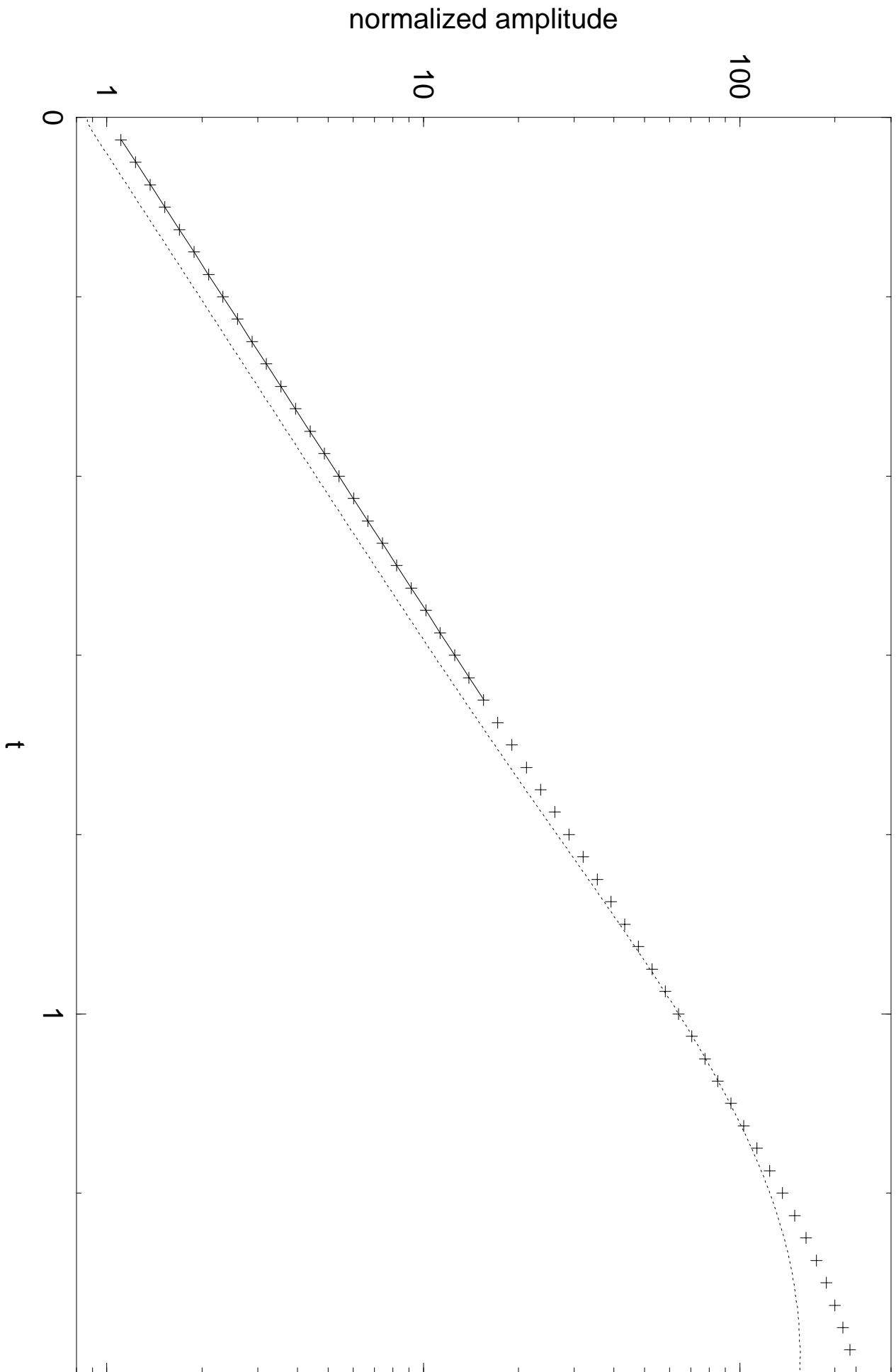


fig. 1

fig. 2

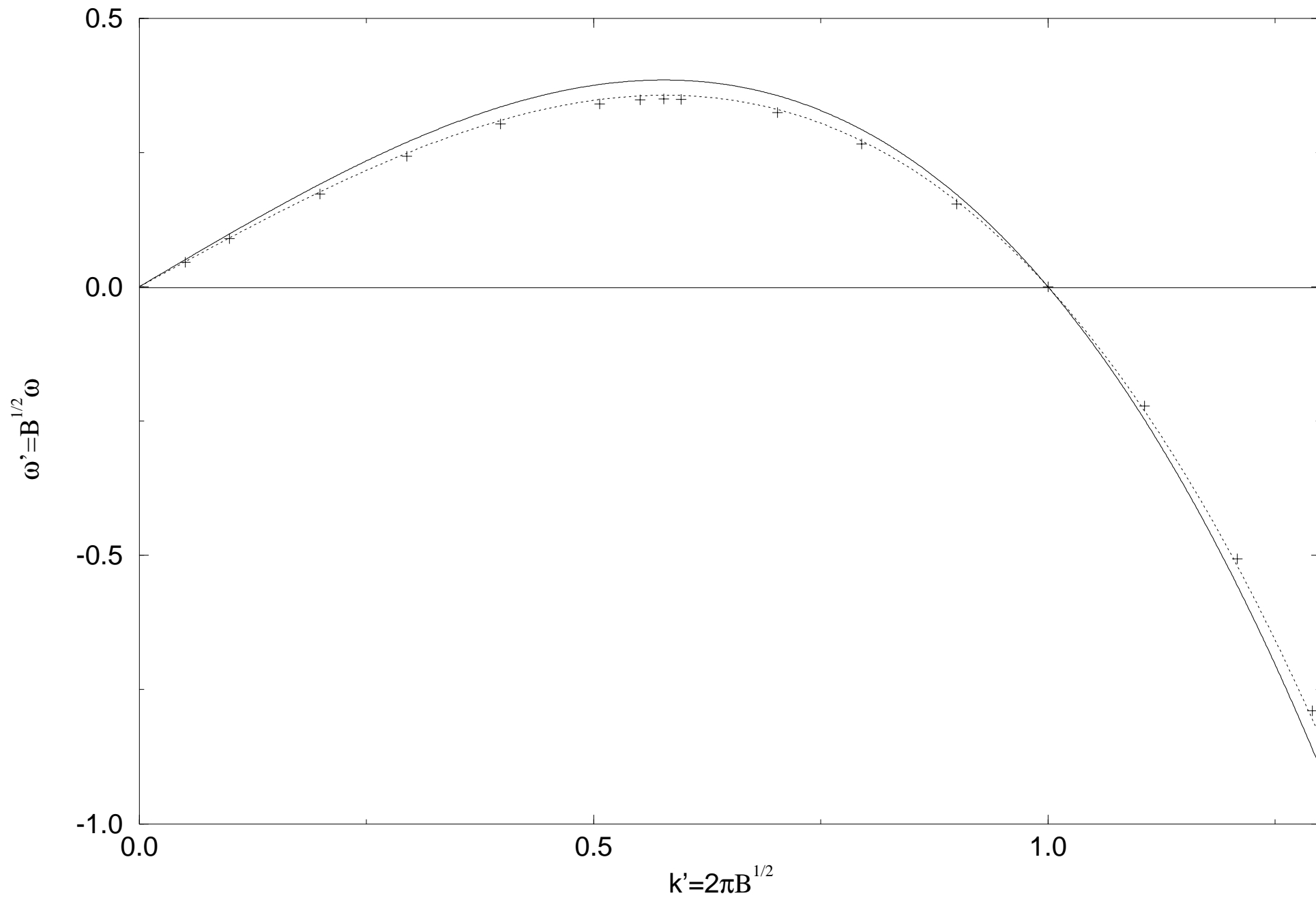


fig. 3

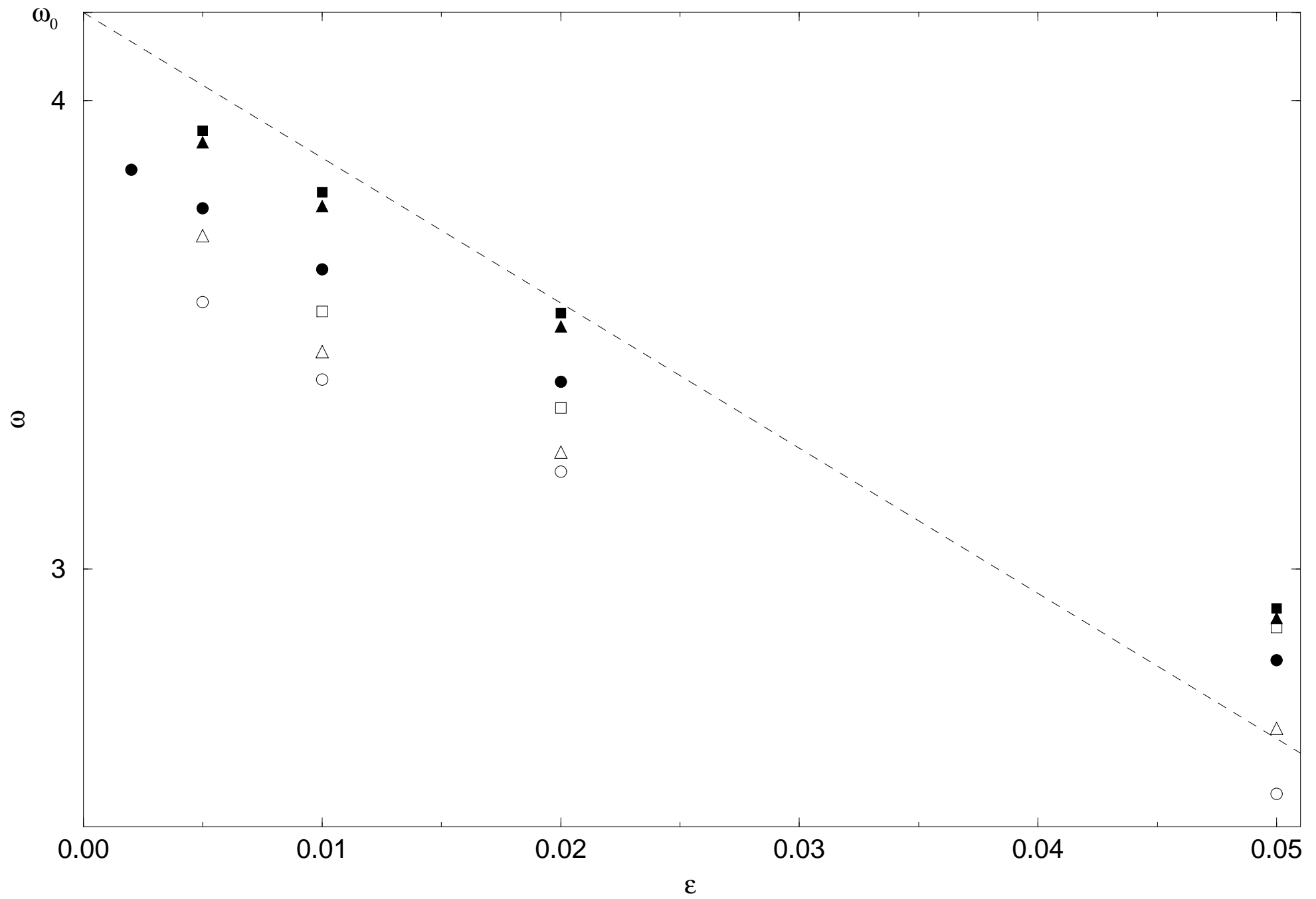


fig. 4.a

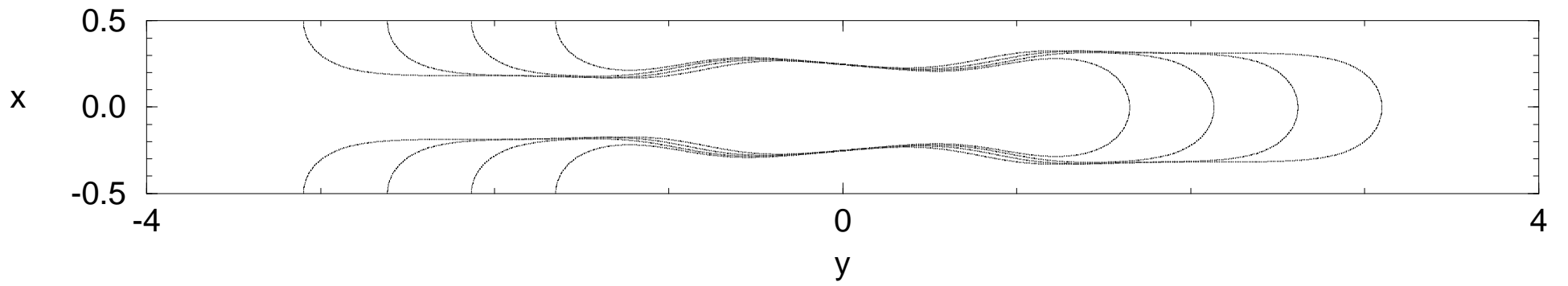


fig. 4.b

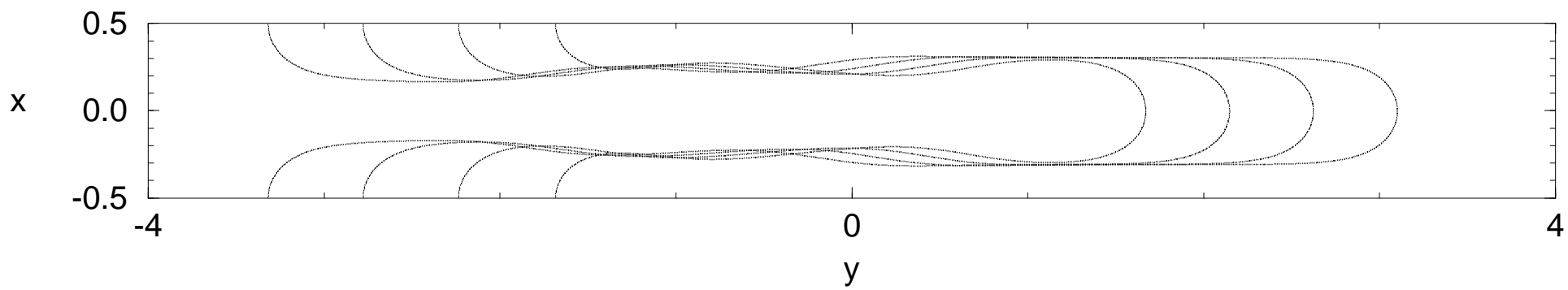


fig. 4.c

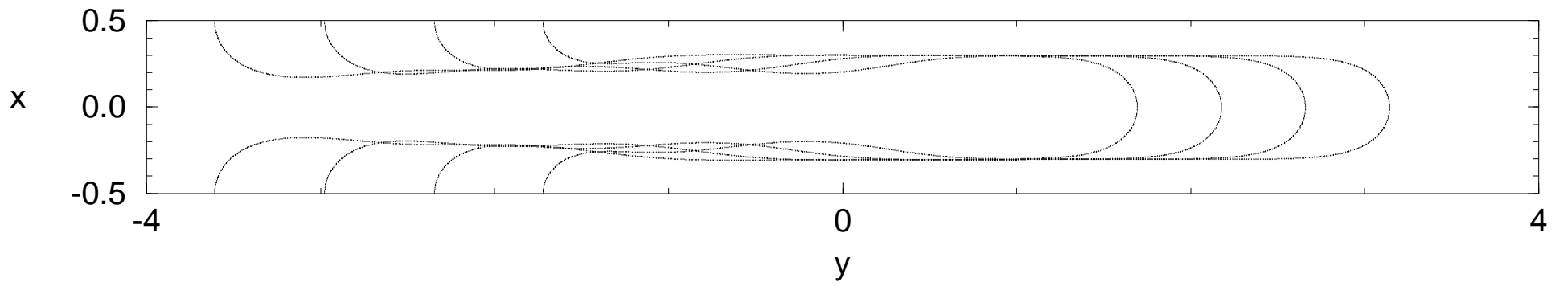


fig. 4.d

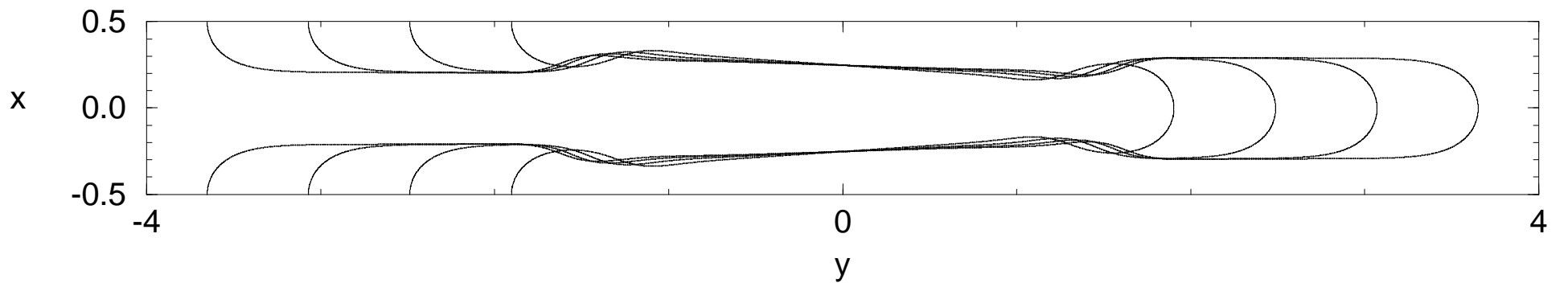


fig. 5.a

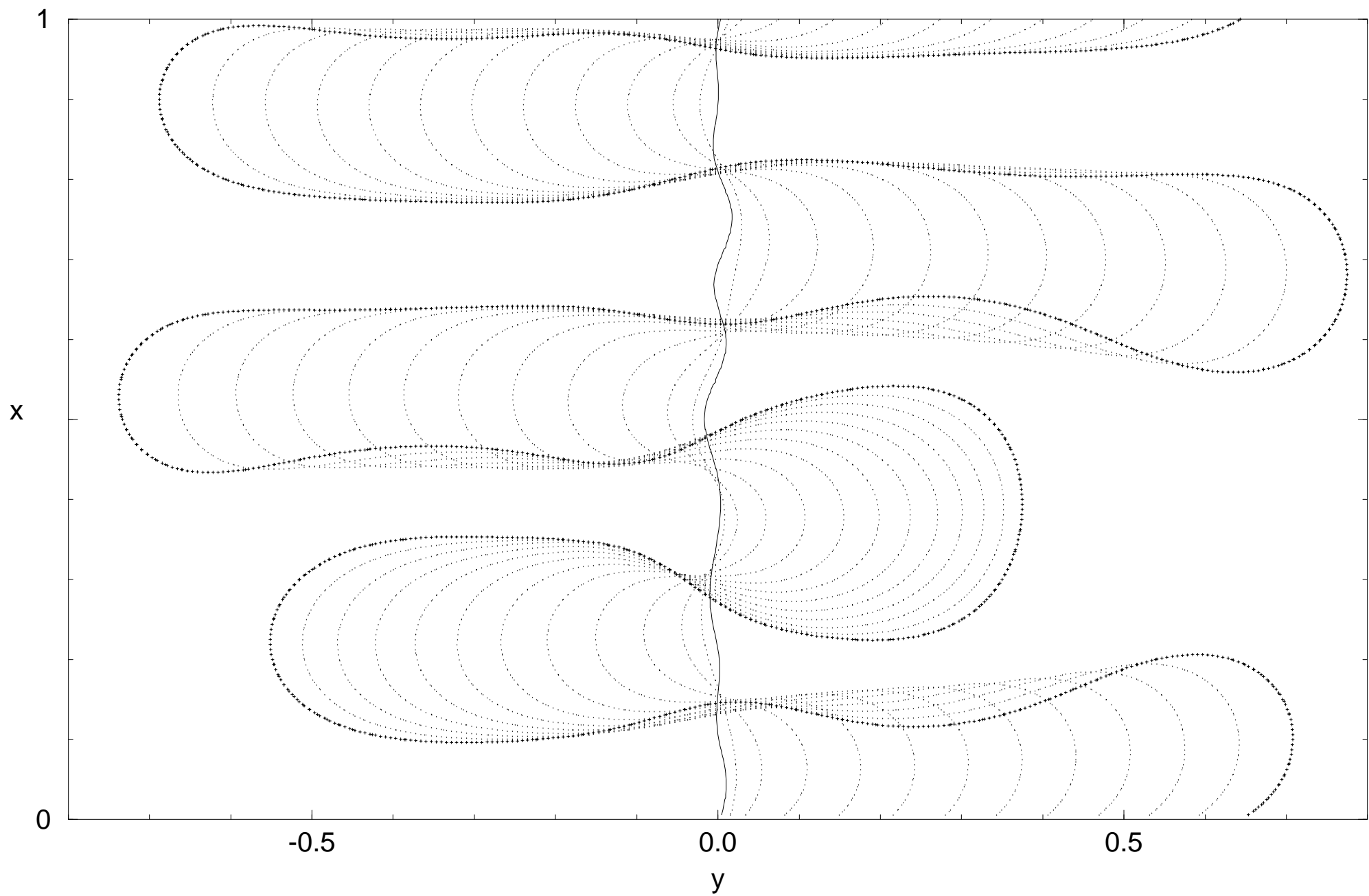


fig. 5.b

